Interfacial-Strain-Induced Structural and Polarization Evolutions in Epitaxial Multiferroic BiFeO$_3$ (001) Thin Films

Haizhong Guo,*,[†] Ruiqiang Zhao,[†] Kui-juan Jin,*,[†,‡] Lin Gu,[†] Dongdong Xiao,[†] Zhenzhong Yang,[†] Xiaolong Li,[§] Le Wang,[†] Xu He,[†] Junxing Gu,[†] Qian Wan,[†] Can Wang,[†] Huibin Lu,[†] Chen Ge,[†] Meng He,[†] and Guozhen Yang[†,‡]

[†]Beijing National Laboratory for Condensed Matter Physics, Institute of Physics, Chinese Academy of Sciences, Beijing 100190, China

[‡]Collaborative Innovation Center of Quantum Matter, Beijing 100190, China

[§]Shanghai Synchrotron Radiation Facility (SSRF), Shanghai Institute of Applied Physics, Chinese Academy of Sciences, Shanghai 201204, China

Ⓢ *Supporting Information*

ABSTRACT: Varying the film thickness is a precise route to tune the interfacial strain to manipulate the properties of the multiferroic materials. Here, to explore the effects of the interfacial strain on the properties of the multiferroic BiFeO$_3$ films, we investigated thickness-dependent structural and polarization evolutions of the BiFeO$_3$ films. The epitaxial growth with an atomic stacking sequence of BiO/TiO$_2$ at the interface was confirmed by scanning transmission electron microscopy. Combining X-ray diffraction experiments and first-principles calculations, a thickness-dependent structural evolution was observed from a fully strained tetragonality to a partially relaxed one without any structural phase transition or rotated twins. The tetragonality (c/a) of the BiFeO$_3$ films increases as the film thickness decreases, while the polarization is in contrast with this trend, and the size effect including the depolarization field plays a crucial role in this contradiction in thinner films. These findings offer an alternative strategy to manipulate structural and polarization properties by tuning the interfacial strain in epitaxial multiferroic thin films.

KEYWORDS: BiFeO$_3$ thin films, interfacial strain, structural evolution, polarization evolution
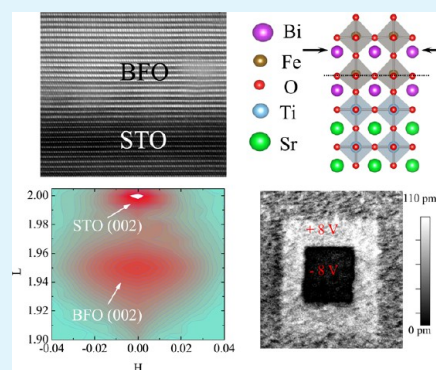
1. INTRODUCTION

Recently, tremendous activities have been engaged to study the multiferroic BiFeO$_3$ (BFO) due to its promising application for magnetoelectric devices as the only known single-phase room-temperature magnetoelectric multiferroic.[1−5] Moreover, BFO is also attractive for mass production from an environmental point of view because of its lead-free nature. The ferroelectric state is realized by a large displacement of the Bi ions relative to the FeO$_6$ octahedra, and the ferroelectric polarization is along the pseudocubic [111] direction, leading to the formation of eight possible polarization variants corresponding to four structural variants.[2−6] Motivation for the growth of epitaxial BFO thin films includes meeting the needs for potential applications in microelectronic and information storage devices. The functional properties of the BFO thin films are strongly sensitive to external parameters, and engineering of epitaxial strain is a powerful tool to tune the material properties with respect to the bulk.[1] Due to the mismatching in lattice parameters or thermal expansion between the films and the substrates, epitaxial strain can be generated and will fracture in bulk form, resulting in properties significantly different from those of the bulk.[1,7−12] Bulk BFO shows a relatively small

spontaneous polarization of 6 μC/cm^2, while BFO thin film structures show large polarization along [111] direction with a magnitude of 90−95 μC/cm^2.[1,7] The structure of bulk BFO is characterized by a rhombohedrally distorted cell with space group $R3c$ and lattice parameters $a = b = c = 3.962$ Å and $\alpha = 89.4°$.[13] However, in the case of thin films, due to the lattice mismatch and thermal expansion between the BFO films and underlying substrates, different states of compressive or tensile strains can be generated by using different underlying substrates, resulting in the different structural phases, from rhombohedral-like monoclinic phase, tetragonal-like monoclinic phase, to a fully relaxed bulklike rhombohedral one.[4,14−24] Recent reports summarized that at in-plane tensile to moderate compressive strain, the BFO films on SrRuO$_3$-buffered substrates are at rhombohedral-like monoclinic phase, while in-plane compressive strains exceeding ~4.5% result in a tetragonal-like monoclinic unit.[4,19] Although monoclinic and rhombohedral phases of BFO films have been extensively

reported, tetragonal phase in BFO films has also been reported in some literature.[14,21,25,26] It is reported that tetragonal phase with giant tetragonality ratio (c/a) has been found in BFO films deposited on La-doped $SrTiO_3$ substrates without any buffer layer,[25] and the tetragonal structure exists in the BFO films grown on $La_{0.67}Sr_{0.33}MnO_3$-buffered STO substrates.[26] Saito et al.[14] found that BFO films grown on $SrRuO_3$-buffered $SrTiO_3$ with a thickness below 50 nm are at tetragonal phase but at monoclinic phase for the film thickness above 50 nm. With increasing growth rate, the crystal structure of epitaxial BFO thin films deposited on $SrRuO_3$-buffered $SrTiO_3$ develops from monoclinic lattice to a mixed phase of two tetragonal lattices with different c/a ratio, finally to a single tetragonal phase.[21] On the other hand, film thickness can be varied to tune epitaxial strain, which modifies the structure and polarization in the BFO thin films.[14,15,17,26,27] It is obvious, therefore, that the crystal structure is strongly dependent on the strain status, that is, substrates as well as film thickness. In this work, to study the effects of the interfacial strain on the properties of the BFO films and to exclude the effects of the buffered layer, we characterized thickness-dependent structural and polarization evolutions of the BFO films on the bare STO substrates with thicknesses from 2 to 449 nm by using high-resolution synchrotron X-ray diffraction (SXRD), scanning transmission electron microscopy (STEM), and piezoresponse force microscopy (PFM).

2. EXPERIMENTAL SECTION

2.1. Fabrication of BFO Films. Epitaxial BFO thin films with various thicknesses of 2, 4, 8, 19, 38, 57, 94, 141, 188, 283, and 449 nm were deposited on (001)-oriented STO and slightly Nb-doped STO single crystals by a laser molecular-beam epitaxy system. The films were deposited at 560 °C using an excimer XeCl laser (1.5 J/cm², 308 nm, 2 Hz) at oxygen pressure of 2 Pa (2×10^{-2} mbar). After deposition, the films were in situ annealed for 30 min then cooled down slowly to room temperature. The detailed growth has also been reported elsewhere.[28−31]

2.2. SXRD, RSM, STEM, and PFM Measurements. The structural phases and out-of-plane lattice constant of the BFO thin films were identified by SXRD at the BL14B1 beamline of Shanghai Synchrotron Radiation Facility (SSRF), using a 1.24 Å X-rays with a Huber 5021 six-axis diffractometry. The crystal structure and lattice parameters of the BFO films have also been investigated by high resolution SXRD reciprocal space mapping (RSM) at the BL14B1 beamline of SSRF. To characterize the crystalline structures of the BFO thin films, state-of-the-art sophisticated aberration-corrected STEM techniques of the high-angle annular dark-field (HAADF) were utilized. The HAADF imaging was executed using an ARM-200F (JEOL, Tokyo, Japan) scanning transmission electron microscope operated at 200 kV with CEOS Cs corrector (CEOS GmbH, Heidelberg, Germany) to cope with the probe-forming objective spherical aberration. The ferroelectric nature of the BFO films on Nb-doped STO substrates was characterized using PFM performed on a commercial atomic force microscope (AFM, Asylum Reasearch MFP-3D). PFM images were collected and recorded using a Ti/Ir-coated Si cantilever (Olympus Electrilever) with a nominal ~2 N/m spring constant and a free air resonance frequency of ~70 kHz.

2.3. First-Principles Calculations. The first-principles calculations were based on the projected augmented wave (PAW)[32] and local spin density approximation (LSDA)[33] + Hubbard U[34] method as implemented in the Vienna ab intio simulation package.[35] The Bi 6s6p, Fe 3d4s, and O 2s2p electrons are considered as valence electrons. A plane wave basis set with the cut off energy of 500 eV was used in the calculation. The U of the Fe atom is selected as 2 eV. The biaxial strain was applied by fixing the in-plane lattice parameters and relaxing the out-of-plane lattice parameter; therefore, no effect of the substrate but the strain was explicitly considered.

3. RESULTS AND DISCUSSION

3.1. Sample Preparation and STEM Characterizations. Epitaxial BFO thin films with various thicknesses were deposited on (001)-oriented $SrTiO_3$ (STO) and slightly Nb:STO single crystals by a laser molecular-beam epitaxy system. Details on film growth are given in the Experimental Section. To characterize the crystalline structures of the BFO thin films, we utilized state-of-the-art sophisticated aberration-corrected STEM techniques of HAADF. Figure 1a shows the
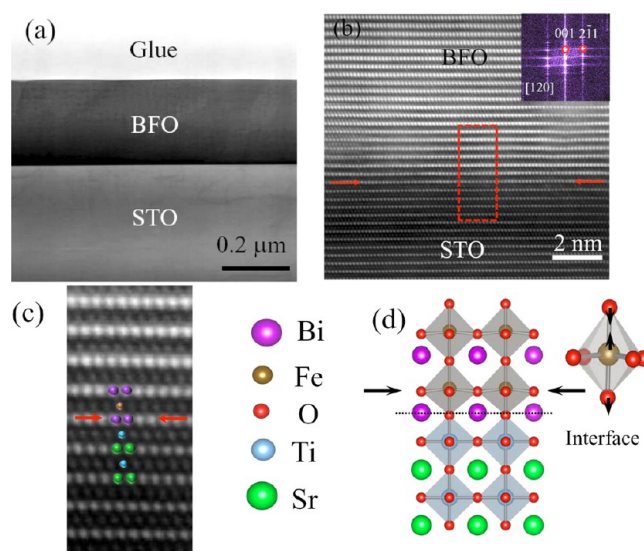
Figure 1. (a) Low-magnification cross-sectional STEM images of the 283 nm thick BFO thin film. (b) Atomically resolved HAADF image of the BFO/STO near the interface along the [120] direction; (inset) FFT pattern of BFO with red arrows marking the interface. (c) Enlarged part of atomically resolved HAADF shown in image b, indicated by the red rectangle, together with the atomic positions of the cations Bi, Fe, Sr, and Ti. (d) The schematic of tetragonal BFO unit cells on cubic STO unit cells and the FeO_6 octahedral with polarized shift.

low-magnification cross-sectional STEM image of the 283 nm thick BFO film grown on the STO substrates. The 283 nm thick BFO film appears flat and homogeneous over large lateral distances, excluding the presence of crystal grains that can contribute to degradation in ferroelectric properties. This point is further confirmed by the high-resolution STEM image near the interface. Figure 1b shows the HAADF imaging near the interface region. An excellent unit-cell to unit-cell epitaxial relationship between the BFO film and STO substrate can be seen in Figure 1b. It also can be observed that the interface is atomically sharp and coherent, without any evidence of secondary phases or chemical reaction in the interface region over large distances. Sharp interface and no buffer layer at the interface of the BFO thin film indicate the epitaxial growth of the BFO thin films on STO and the high epitaxial quality of our BFO thin films. The fast Fourier transform (FFT) pattern of the BFO film, shown in the inset of Figure 1b, corresponds to the tetragonal structure (P4mm). The enlarged part of atomically resolved HAADF image near the interface is shown in Figure 1c. From Figure 1c, it is very clear that the atomic stacking sequence at the interface is BiO/TiO_2, further confirming the epitaxial growth the BFO films on the TiO_2-terminated STO substrates. Figure 1d shows the schematic of

tetragonal BFO unit cells on cubic STO unit cells and the FeO_6 octahedral with polarized shift.

3.2. Structural Evolutions Investigated by SXRD and RSM.

The high-resolution SXRD $\theta-2\theta$ scan curves of the BFO thin films with different thicknesses are shown in Figure 2a.
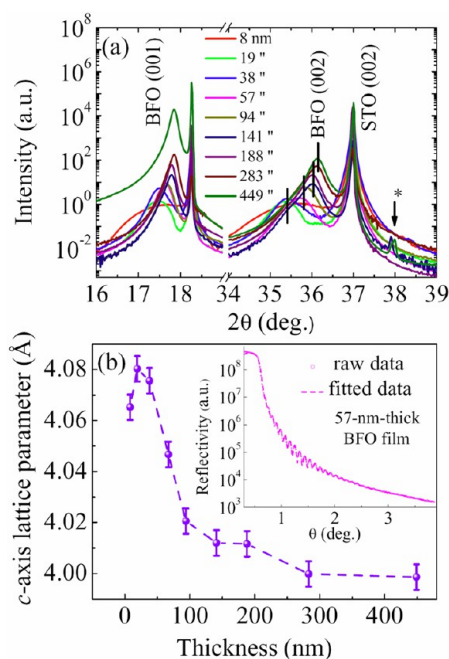
Figure 2. (a) SXRD $\theta-2\theta$ scan curves of the BFO thin films with different thicknesses of 8, 19, 38, 57, 94, 141, 188, 283, and 449 nm, respectively; (b) c axis lattice parameter as a function of BFO thickness; (inset, solid line) X-ray reflectivity profile with (dashed line) the fitted result of the 57 nm thick BFO thin film.

The $(00l)$ reflections from the films are observed in addition to the substrate peaks, suggesting that the thin films have same orientation with the substrate, that is, c axis orientation. Moreover, it can be seen from Figure 2a that with the film thickness within the region of 19−94 nm, single-phase BFO films can be obtained. However, once film thickness is larger than 141 nm, an extra weak peak (marked with an asterisk) attributed to Fe_2O_3 phase can be detected. It was well-known that the growth window of phase-pure BFO thin films is very small, and both temperature and oxygen pressure affect the film quality and phase purity significantly, as shown in the pressure−temperature phase diagram for BFO deposition mapped out by Béa et al.[20] Our SXRD results demonstrate that even within the window where phase pure BFO thin films can be obtained (560 °C, 2×10^{-2} mbar), a small amount of parasitic phases exist when film thickness is larger than a certain thickness (such as 141 nm in present work). The c lattice parameter is shown in Figure 2b as a function of the BFO film thickness. It can be seen from Figure 2a that the c axis lattice parameter decreases rapidly with increasing the film thickness up to 94 nm, and then decreases slowly and almost keeps constantly over 141 nm. The inset of Figure 2b shows a typical experimental reflectivity profile together with the fitted profile for the 57 nm thick BFO thin film. The interference (Kiessig) fringes are clearly present in the profile. The precise determination of the film thickness was obtained by fitting the periodicity of the Kiessig interference fringes.

The high-resolution SXRD reciprocal space mapping (RSM) is plotted in reciprocal lattice units (r.l.u.) of the STO substrate (1r.l.u. = $2\pi/3.905$ Å^{-1}). Figure 3a1−f1 shows the high-resolution HL RSMs around the (002) STO diffraction peak of the BFO films with the thicknesses of 8, 57, 94, 141, 188, and 449 nm, respectively. H, K, and L are reciprocal space coordinates. It can be seen from Figure 3a1−f1 that all BFO RSM spots almost have the same H values as that of the STO substrate, indicating that the (001) planes of BFO films are parallel to the STO substrate and the BFO films with different thicknesses were grown coherently on the STO substrates, as $(00l)BFO//(00l)STO$, consistent with the STEM results. To further characterize the crystal structure of BFO films of varying thickness, we also measured KH RSM around (002) BFO diffraction for BFO films with film thicknesses of 8, 57, 94, 141, 188, and 449 nm, as shown in Figure 3a2−f2. These RSMs were obtained with L values at the BFO peaks in Figure 3a1−f1. It can be clearly seen from Figure 3a2−f2 that single peak structure without any other structure was observed around BFO (002) peak with BFO film thickness varying from 8 to 449 nm, indicating that there is no existence of the rotated twinning structure or structural grains of the BFO lattice even with the BFO film thickness as large as 449 nm.

RSMs around (002) only show the information on the spacing of lattice planes in the out-of-plane direction, and RSM diffraction patterns around other diffractions will prove more information on the crystal structure and lattice parameters. Therefore, RSM diffraction patterns around (103) STO and (113) STO were also measured, and the high-resolution HL RSMs around the (103) STO reflection and KH RSMs around (103) BFO diffraction are shown in Figure S1(Supporting Information). It can be seen from Figure S1a1−f1 (Supporting Information) that all BFO RSM spots around (103) diffraction exhibit single-peak structure, indicating a tetragonal lattice for all BFO films with different thicknesses.[14] It can also be clearly seen from Figure S1a2−f2 (Supporting Information) that the single peak of KH RSMs is around the (103) BFO diffraction structure, further confirming that there is no existence of the rotated twinning structure of the BFO lattice in our BFO films. To confirm the tetragonal phase of the BFO films, we also performed the RSMs around STO (103), (013), and (0$\bar{1}$3) diffraction peaks of the 188 nm thick BFO film, as shown in Figure 2S. The RSMs results of Figure 2S show that the symmetrical/equivalent positions of these peaks around (103), (013), and (0$\bar{1}$3) reflection peaks, further confirming no existence of the rotated twinning structure in the BFO films and the tetragonal phase of the BFO films.

Our RSMs results differ from the previous reports on the thickness-dependent structural evolution of the BFO (001) films deposited on $SrRuO_3$ (SRO)-buffered STO substrates, in which the BFO (002) peak splits into two peaks along the H (or K) direction due to the evolution of the rotated twin-structure when the BFO film thickness is larger than 200 nm.[4,5,16−19,22−24] The structure of bulk BFO is characterized by a rhombohedral unit cell with space group $R3c$ and lattice parameters[13] $a_{BFO} = 3.962$ Å and $\alpha_{BFO} = 89.4°$, and a_{BFO} is slightly larger than the lattice parameter a_{STO} of STO ($a_{STO} = 3.905$ Å); therefore, an epitaxial in-plane compressive strain in the BFO films will generate from the substrate mismatch and gradually relax with increasing the thicknesses of the BFO films when BFO films are epitaxially grown on the STO substrates. Due to the coherently epitaxial growth of BFO films on the STO substrates within the optimal conditions where phase-
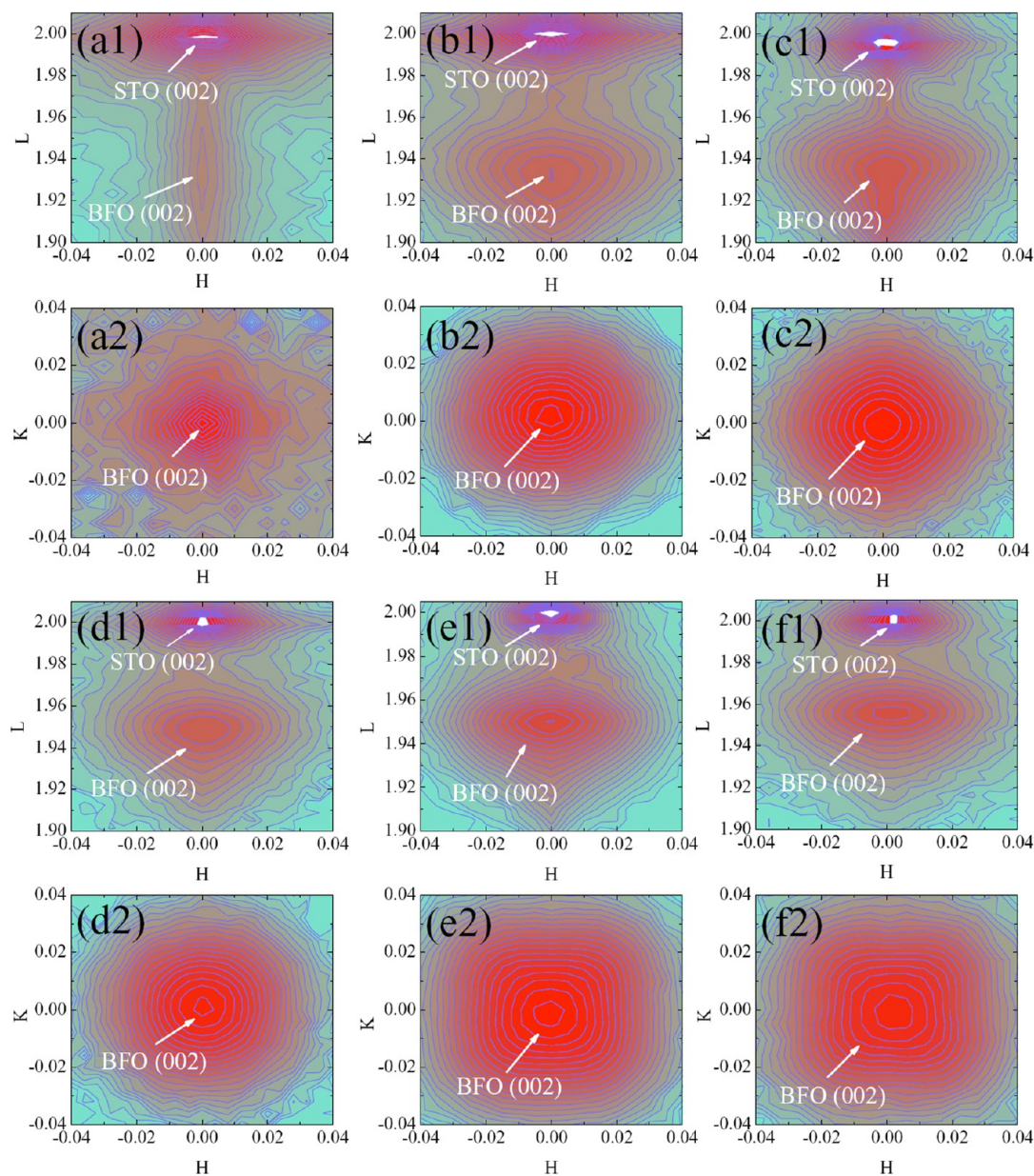
Figure 3. *HL* reciprocal space mappings around STO (002) for the BFO films with film thicknesses of (a1) 8, (b1) 57, (c1) 94, (d1) 141, (e1) 188, and (f1) 449 nm. *KH* reciprocal space mappings around BFO (002) for the BFO films with film thicknesses of (a2) 8, (b2) 57, (c2) 94, (d2) 141, (e2) 188, and (f2) 449 nm.

pure BFO thin films can be obtained (560 °C, 2 × 10⁻² mbar), coherent tetragonal phase in BFO films will be stable on STO substrates, and the rotated twinning structure of the BFO lattice does not develop in our BFO films, even the BFO film thickness as large as 449 nm. SRO bulk has an orthorhombic structure with a_{SRO} = 5.574 Å, b_{SRO} = 5.541 Å nm and c_{SRO} = 7.785 Å.[25] For many simple geometric considerations, it is sufficient to refer to a pseudocubic cell with a cell parameter of 3.941 nm. This parameter is slightly larger than that of STO but smaller than that of BFO. Therefore, in the BFO/SRO/STO bilayer, as the thin SRO buffer layer and STO substrate are rather close in lattice parameters, compared to the lattice parameters between BFO and STO, the lattice mismatch between BFO and STO will be partially relaxed in SRO buffer layer, and then it will continue to be released partially as a result of the rotation in twinning structure of BFO films with increasing the thicknesses of the BFO films.[4,5,16−19,22−24]

From the RSM results around BFO (002), (103), and (113) peaks, the crystal structures and lattice parameters were determined. From the results of the RSMs it is indicated that the tetragonal lattice does not change for our BFO films grown directly on the STO substrates varying the thicknesses from 2 to 449 nm, and there is no existence of other structural grains or the rotated twinning structure of the BFO lattice in our BFO films. Figure 4 summarizes the relationships of the thicknesses and the out-of-plane and in-plane lattice parameters, the c/a parameters ratio, and the strain of the BFO films with varying thicknesses from 2 to 449 nm, respectively. Due to the lattice mismatch between BFO (3.962 Å) and STO (3.905 Å), in-plane compressive strain and out-of-plane tensile strain will exist in the BFO films, and the BFO lattice is compressed in the in-plane direction and elongated in the out-of-plane direction. It can be seen from Figure 4a that the lattice parameters (*a* and *c*) change dramatically with increasing film thickness up to 94
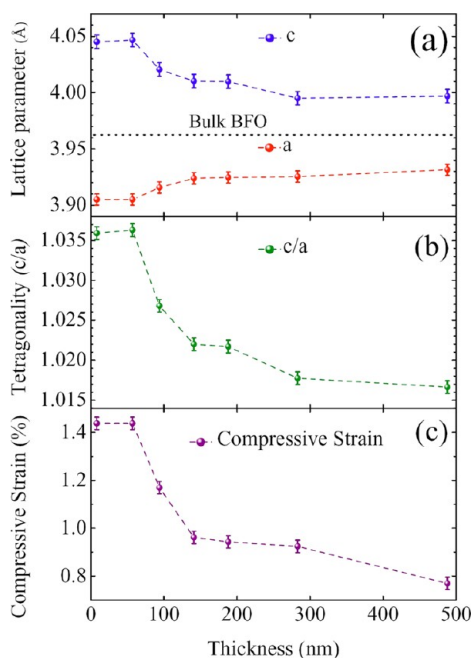
Figure 4. Thickness-dependent (a) out-of-plane and in-plane lattice parameters, (b) c/a lattice parameter ratio, and (c) in-plane compressive strain.

Figure 5. (a, lines) Calculated and (dots) experimental out-of-plane lattice parameter and c/a ratio as a function of the in-plane compressive strain. (b) Calculated free energy as a function of the in-plane compressive strain for tetragonal ($P4mm$) and monoclinic (Cc) phases.

nm and then change slowly over 141 nm. Moreover, the out-of-plane parameter of the BFO films is larger than that of the bulk, and the in-plane lattice parameter is smaller than that of the bulk, even for the BFO films over 141 nm. Correspondingly, the c/a (Figure 4b) decreases dramatically with increasing the BFO thickness until up to 141 nm, and then decreases slightly with further increasing the BFO thickness. The obtained c/a (1.015−1.036) value for the BFO films with tetragonal unit cells is close to those of previous reports,[21,26] much smaller than that of giant tetragonal-like (monoclinic M_C) c/a ratio around 1.23.[4,16] The in-plane compressive strain as the function of the BFO thickness is shown in Figure 4c. It can be seen from Figure 4c that the fully epitaxial and strained BFO films have been created in very thin films (<40 nm), and in-plane compressive strain gradually decreases with the increase of film thickness. Even in the thickest film (∼449 nm) in our work, the strain does not relax fully.

3.3. Theoretical Calculation of the Structural Evolutions. To get a better insight into the experimental data at the atomic level, we performed first-principles calculations. The lattice parameters and the free energy as a function of the in-plane compressive strain were obtained from the first-principles calculations, as shown in Figure 5a,b. It is obvious from Figure 5a that the calculated out-of-plane lattice parameter and c/a ratio for tetragonal structure ($P4mm$) increase with increasing the in-plane compressive strain, and the experimental data are in good agreement with the calculated results, which therefore suggests that all the BFO thin films on the STO substrates are at tetragonal phase with thicknesses varying from 2 to 449 nm. It is very clear from Figure 5b that the free energy of tetragonal ($P4mm$) symmetry is larger than that of monoclinic (Cc) phase, indicating that the monoclinic (Cc) phase is energetically more favorable than the purely tetragonal ($P4mm$) in the BFO thin films, as reported by theoretical investigation and experimental results.[4,16,20,36] Even so, our BFO films on the STO substrates
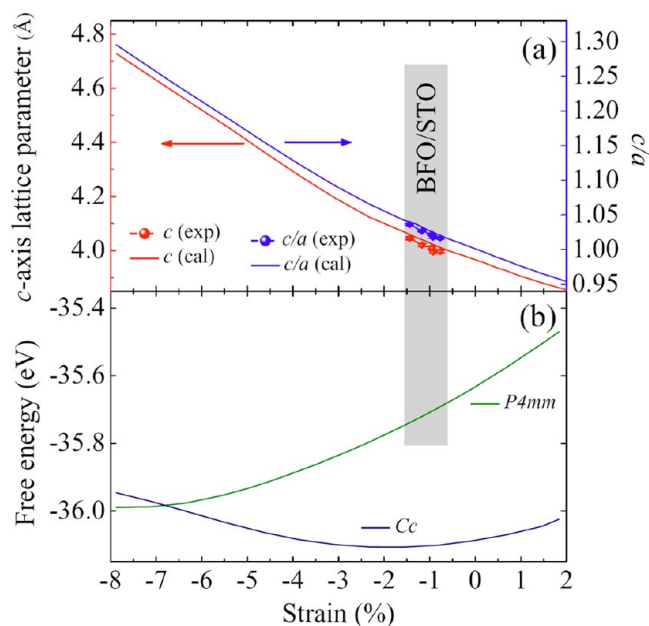
can maintain stably at tetragonal phase due to the compressive strain.

3.4. Polarization Evolutions Investigated by PFM. The ferroelectric nature of the BFO films on Nb:STO was characterized using PFM. Figure 6a,d represents the atomic force microscope (AFM) topography images of the 8 nm thick and 57 nm thick BFO films, respectively. The BFO films with thicknesses of 8 and 57 nm exhibit atomically smooth surfaces with a root-mean-square roughness of approximately 0.32 and 0.47 nm over an area of 3 × 3 μm, respectively, which reduce any rough surface ambiguities during the PFM measurement. Out-of-plane PFM amplitudes and phase images of ferroelectric domains written on the BFO surfaces are shown in Figure 6b,c,e,f. A clear contrast between up and down ferroelectric domains is observed in the BFO films, and the PFM phases can be reversibly switched from 0° to ∼ 180°, which demonstrates the ferroelectric character in both the 8 nm thick and the 57 nm thick BFO films.

The local ferroelectric switching PFM amplitude and phase data of the BFO films on Nb:STO with the thicknesses from 18 to 449 nm were also investigated by PFM, as shown in Figures 7a−e. Extremely sharp polarization switching is observed for all the BFO films in the phase loops with almost 180° phase change. The value of the piezoelectric coefficient d_{33} derived from the PFM amplitude data increases with the film thickness, as shown in Figure 7f, consistent with the results of the previous reports.[1] Our previous work on the BiFeO$_3$/La$_{0.7}$Sr$_{0.3}$MnO$_3$/SrTiO$_3$ bilayer also demonstrates that the dielectric permittivity and remnant polarization increase with the thickness of the BFO layer.[28] Our SXRD results demonstrate that a small amount Fe$_2$O$_3$ phase exists when film thickness is larger than 141 nm. Fe$_2$O$_3$ does not show ferroelectric properties, and the small amount of impure phase Fe$_2$O$_3$ in the BFO films has slight effect on its ferroelectric properties. It is reported that the BFO films with a small
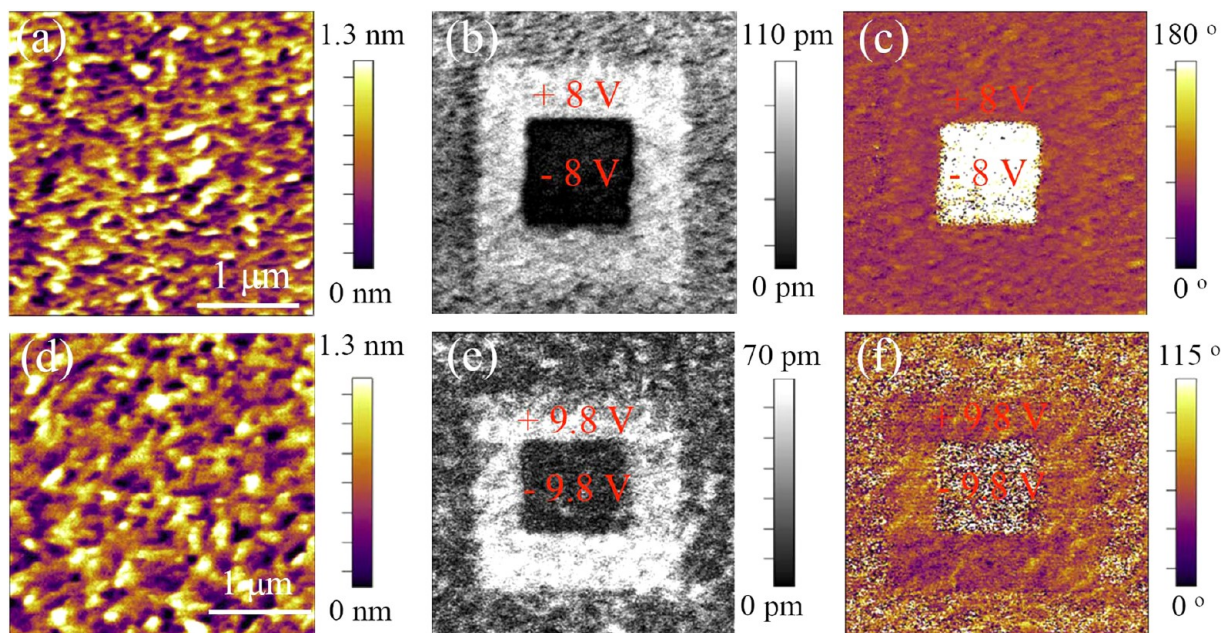
Figure 6. Morphology of the surface of the (a) 8 nm thick and (d) 57 nm thick BFO films measured by AFM with an area of 3×3 μm; PFM out-of-plane amplitude images of the (b) 8 nm thick and (e) 57 nm thick BFO films; PFM out-of-plane phase images of the (c) 8 nm thick and (f) 57 nm thick BFO films. PFM out-of-plane amplitude and images taken over the same area measured by AFM after application of ± 8 V and ± 9.8 V writing voltage on the 8 nm thick and 57 nm thick BFO films, respectively, indicating ferroelectric switching occurring in these films.
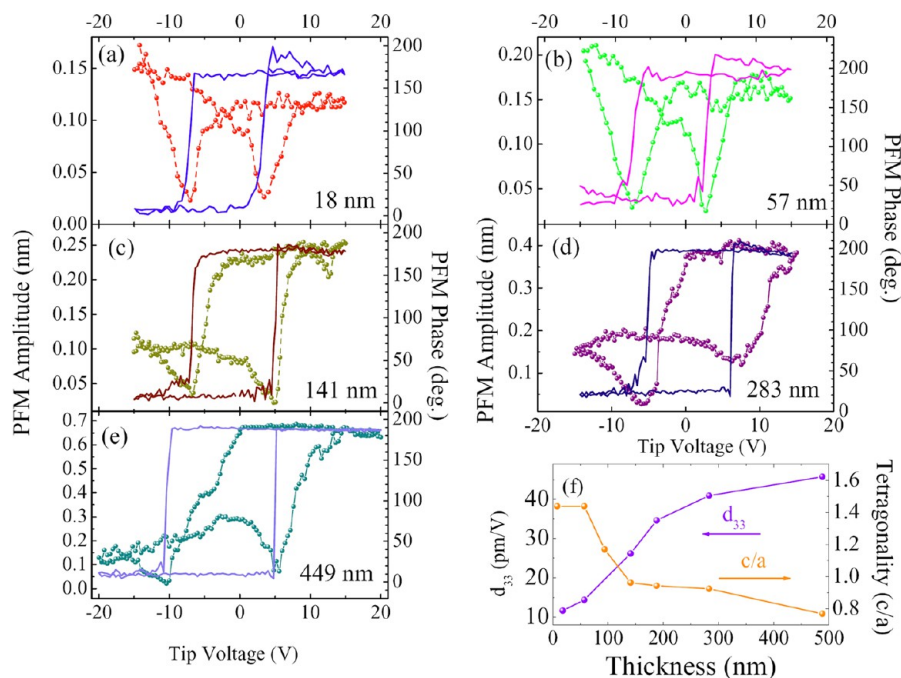
Figure 7. Local switching-spectroscopy (dot) PFM amplitude and (line) PFM phase data of (a) 18 nm thick BFO film, (b) 57 nm thick BFO film, (c) 141 nm thick BFO film, (d) 283 nm thick BFO film, and (e) 449 nm thick BFO film; (f) piezoelectric coefficient d_{33} and tetragonality as a function of the thickness.

amount of impure Fe_2O_3 have lower the polarization values comparing with pure BFO films.[37] Therefore, the increase of the value of the piezoelectric coefficient d_{33} for thicker films cannot be due to the small amount of impure phase Fe_2O_3 in the BFO films.

From SXRD results, we know that the tetragonality (c/a) decreases as the BFO thickness increases, as shown in Figures 5b and 7f, whereas the evolution of the polarization of the BFO films on the Nb:STO substrates is contrary with this trend. Typically, ferroelectric polarization and strain in ferroelectric materials are coupled, leading to the generally accepted direct relation between polarization and tetragonality, such as in $PbTiO_3$ thin films on Nb:STO substrates.[38] Similar contradiction of the relation between polarization and tetragonality was also found in the BFO films on the $La_{0.67}Sr_{0.33}MnO_3$-buffered STO substrates with constant tetragonality, in which

the polarization drops abruptly below a critical thickness, whereas the tetragonality has a high constant value.[26] The contradiction between the tetragonality and the polarization was also observed in the $SrRuO_3/PbZr_{0.2}Ti_{0.8}O_3/SrRuO_3/SrTiO_3$ heterostructures.[39] The size effect including the depolarization field has been identified as a crucial factor for this contradiction between the tetragonality and the polarization. The size effect is largely driven by the concept of a correlation volume, which is related to the required number of aligned dipoles for ferroelectricity to occur. As a film becomes thicker, there are more aligned dipoles contributing to the ferroelectricity, and then the polarization becomes larger. Instability of the ferroelectric phase might be expected for films below a certain thickness when reducing the sample size. Another reason may come from the depolarization field arising from uncompensated surface charges, and the depolarization field will reduce or even suppress ferroelectricity below a critical thickness.[40] For example, Rault et al.[26] used a first-principles-based effective Hamiltonian approach to explain the contradiction between the tetragonality and ferroelectricity, and they proposed that, as a function of screening, the BFO ultrathin films undergo a phase transition from single to nanoscale stripe domains with an overall out-plane polarization close to zero while maintaining the relatively large tetragonal distortion imposed by nonzero polarization state of each individual domain. Nagarajan et al.[39] also used the first-principles simulations to predict the formation of a 180° polydomain state for the thinnest films due to the presence a residual depolarization field. However, the origin of the contradiction between the tetragonality and ferroelectricity as the function of the thickness is still under debate.

4. CONCLUSIONS

In summary, BFO thin films with the thicknesses varying from 2 to 449 nm were epitaxially deposited on the STO and Nb:STO (001) substrates, and interfacial-strain-induced structural and polarization evolutions as a function of thickness were investigated. As the film thickness was increased from 2 to 449 nm, a thickness-dependent structural evolution was observed from a fully strained tetragonality to a partially relaxed one without any structural phase transition or rotated twins. The polarization of the BFO films increases with thickness, contradicting the trend of the tetragonality (c/a), which was suggested to originate from the depolarization field. These findings offer an alternative strategy to manipulate structural and polarization properties by tuning the interfacial strain in epitaxial multiferroic thin films.

■ ASSOCIATED CONTENT

ⓢ Supporting Information

High-resolution *HL* RSMs around the (103) STO reflection and *HK* RSMs around (103) BFO diffraction; *HL* RSMs around STO (013), (013), and (0−13), together with *HK* RSMs around BFO (103), (013), and (0−13) for the 188 nm thick BFO film; calculated structure of the $BiFeO_3$ in *P4mm* phase; calculated internal coordinates along the z direction; coordinates of the atoms along the z direction; and calculated Born effective charges of the atoms. This material is available free of charge via the Internet at http://pubs.acs.org.

■ AUTHOR INFORMATION

Corresponding Authors
*E-mail: hguo@iphy.ac.cn.
*E-mail: kjjin@iphy.ac.cn.

■ ABBREVIATIONS

BFO, $BiFeO_3$
STO, $SrTiO_3$
Nb:STO, Nb-doped $SrTiO_3$
SXRD, synchrotron X-ray diffractometry
SSRF, Shanghai Synchrotron Radiation Facility
RSM, reciprocal space mapping
STEM, scanning transmission electron microscopy
HAADF, high-angle annular dark field
AFM, atomic force microscope
PFM, piezoresponse force microscopy

■ REFERENCES

(1) Wang, J.; Neaton, J. B.; Zheng, H.; Nagarajan, V.; Ogale, S. B.; Liu, B.; Viehland, D.; Vaithyanathan, V.; Schlom, D. G.; Waghmare, U. V.; Spaldin, N. A.; Rabe, K. M.; Wuttig, M.; Ramesh, R. Epitaxial $BiFeO_3$ Multiferroic Thin Film Heterostructures. *Science* 2003, 299, 1719−1722.

(2) Zhao, T.; Scholl, A.; Zavaliche, F.; Lee, K.; Barry, M.; Doran, A.; Cruz, M. P.; Chu, Y. H.; Ederer, C.; Spaldin, N. A.; Das, R. R.; Kim, D. M.; Baek, S. H.; Eom, C. B.; Ramesh, R. Electrical Control of Antiferromagnetic Domains in Multiferroic $BiFeO_3$ Films at Room Temperature. *Nat. Mater.* 2006, 5, 823−829.

(3) Jiang, K.; Zhu, J. J.; Wu, J. D.; Sun, J.; Hu, Z. G.; Chu, J. H. Influences of Oxygen Pressure on Optical Properties and Interband Electronic Transitions in Multiferroic Bismuth Ferrite Nanocrystalline Films Grown by Pulsed Laser Deposition. *ACS Appl. Mater. Interfaces* 2011, 3, 4844−4852.

(4) Chen, Z.; Luo, Z.; Huang, C.; Qi, Y.; Yang, P.; You, L.; Hu, C.; Wu, T.; Wang, J.; Gao, C.; Sritharan, T.; Chen, L. Low-Symmetry Monoclinic Phase and Polarization Rotation Path Mediated by Epitaxial Strain in Multiferroic $BiFeO_3$ Thin Films. *Adv. Funct. Mater.* 2011, 21, 133−138.

(5) Jang, H. W.; Ortiz, D.; Baek, S.; Folkman, C. M.; Das, R. R.; Shafer, P.; Chen, Y.; Nelson, C. T.; Pan, X.; Ramesh, R.; Eom, C. Domain Engineering for Enhanced Ferroelectric Properties of Epitaxial (001) BiFeO Thin Films. *Adv. Mater.* 2009, 21, 817−823.

(6) Wu, J.; Wang, J.; Xiao, D.; Zhu, J. A Method to Improve Electrical Properties of BiFeO₃ Thin Films. *ACS Appl. Mater. Interfaces* **2012**, *4*, 1182−1185.

(7) Bai, F.; Wang, J.; Wuttig, M.; Li, J.; Wang, N.; Pyatakov, A. P.; Zvezdin, A. K.; Cross, L. E.; Viehland, D. Destruction of Spin Cycloid in (111)$_C$-Oriented BiFeO₃ Thin Films by Epitiaxial Constraint: Enhanced Polarization and Release of Latent Magnetization. *Appl. Phys. Lett.* **2005**, *86*, 032511.

(8) Andrés, J.; Gracia, L.; Gonzalez-Navarrete, P.; Longo, V. M.; Avansi, W., Jr.; Volanti, W. P.; Ferrer, M. M.; Lemos, P. S.; La Porta, F. A.; Hernandes, A. C.; Longo, E. Structural and Electronic Analysis of the Atomic Scale Nucleation of Ag on α-Ag₂WO₄ Induced by Electron Irradiation. *Sci. Rep.* **2014**, *4*, 5391.

(9) Algueró, M.; Ricote, J.; Torres, M.; Amorín, H.; Alberca, A.; Iglesias-Freire, O.; Nemes, N.; Holgado, S.; Cervera, M.; Piqueras, J.; Asenjo, A.; García-Hernández, M. Thin Film Multiferroic Nanocomposites by Ion Implantation. *ACS Appl. Mater. Interfaces* **2014**, *6*, 1909−1915.

(10) MacManus-Driscoll, J. L. Self-Assembled Heteroepitaxial Oxide Nanocomposite Thin Film Structures: Designing Interface-Induced Functionality in Electronic Materials. *Adv. Funct. Mater.* **2010**, *20*, 2035−2045.

(11) Fusil, S.; Garcia, V.; Barthélémy, A.; Bibes, M. Magnetoelectric Devices for Spintronics. *Annu. Rev. Mater. Res.* **2014**, *44*, 91−116.

(12) La Porta, F. A.; Andrés, J.; Vismara, M. V. G.; Graeff, C. F. O.; Sambrano, J. R.; Li, M. S.; Varela, J. A.; Longo, E. Correlation Between Structural and Electronic Order−Disorder Effects and Optical Properties in ZnO Nanocrystals. *J. Mater. Chem. C* **2014**, *2*, 10164−10174.

(13) Michel, C.; Moreau, J. M.; Achenbach, G. D.; Gerson, R.; James, W. J. The Atomic Structure of BiFeO₃. *Solid State Commun.* **1969**, *7*, 701−704.

(14) Saito, K.; Ulyanenkov, A.; Grossmann, V.; Ress, H.; Bruegemann, L.; Ohta, H.; Kurosawa, T.; Ueki, S.; Funakubo, H. Structural Characterization of BiFeO₃ Thin Films by Reciprocal Space Mapping. *Jpn. J. Appl. Phys.* **2006**, *45*, 7311−7314.

(15) Mazumdar, D.; Shelke, V.; Iliev, M.; Jesse, S.; Kumar, A.; Kalinin, S. V.; Baddorf, A. P.; Gupta, A. Nanoscale Switching Characteristics of Nearly Tetragonal BiFeO₃ Thin Films. *Nano Lett.* **2010**, *10*, 2555−2561.

(16) Zeches, R. J.; Rossell, M. D.; Zhang, J. X.; Hatt, A. J.; He, Q.; Yang, C.-H.; Kumar, A.; Wang, C. H.; Melville, A.; Adamo, C.; Sheng, G.; Chu, Y.-H.; Ihlefeld, J. F.; Erni, R.; Ederer, C.; Gopalan, V.; Chen, L. Q.; Schom, D. G.; Spaldin, N. A.; Martin, L. W.; Ramesh, R. A Strain-Driven Morphotropic Phase Boundary in BiFeO₃. *Science* **2009**, *326*, 977−980.

(17) Liu, H.; Yao, K.; Yang, P.; Du, Y.; He, Q.; Gu, Y.; Li, X.; Wang, S.; Zhou, X.; Wang, J. Thickness-Dependent Twinning Evolution and Ferroelectric Behavior of Epitaxial BiFeO₃ (001) Thin Films. *Phys. Rev. B* **2010**, *82*, 064108.

(18) Jang, H. W.; Baek, S. H.; Ortiz, D.; Folkman, C. M.; Das, R. R.; Chu, Y. H.; Shafer, P.; Zhang, J. X.; Choudhury, S.; Vaithyanathan, V.; Chen, Y. B.; Felker, D. A.; Biegalski, M. D.; Rzchowski, M. S.; Pan, X. Q.; Schlom, D. G.; Chen, L. Q.; Ramesh, R.; Eom, C. B. Strain-Induced Polarization Rotation in Epitaxial (001) Thin Films. *Phys. Rev. Lett.* **2008**, *101*, 107602.

(19) Christen, H. M.; Nam, J. H.; Kim, H. S.; Hatt, A. J.; Spaldin, N. A. Stress-Induced $R−M_A−M_C−T$ Symmetry Changes in BiFeO₃ Films. *Phys. Rev. B* **2011**, *83*, 144107.

(20) Béa, H.; Bibes, M.; Barthélémy, A.; Bouzehouane, K.; Jacquet, E.; Khodan, A.; Contour, J.-P.; Fusil, S.; Wyczisk, F.; Forget, A.; Lebeugle, D.; Colson, D.; Viret, M. Influence of Parasitic Phase on the Properties of BiFeO₃ Epitaxial Thin Films. *Appl. Phys. Lett.* **2005**, *87*, 072508.

(21) Liu, H.; Yang, P.; Yao, K.; Wang, J. Growth Rate Induced Monoclinic to Tetragonic Phase Transition in Epitaxial BiFeO₃ (001) Thin Films. *Appl. Phys. Lett.* **2011**, *98*, 102902.

(22) Liu, H.; Yang, P.; Yao, K.; Wang, J. Twinning Rotation and Ferroelectric Behavior of Epitaxial BiFeO₃ (001) Thin Film. *Appl. Phys. Lett.* **2010**, *96*, 012901.

(23) Xu, G.; Hiraka, H.; Shirane, G.; Li, J.; Wang, J.; Viehland, D. Low Symmetry Phase in (001) BiFeO₃ Epitaxial Constrained Thin Films. *Appl. Phys. Lett.* **2005**, *86*, 182905.

(24) Qi, X.; Wi, M.; Lin, Y.; Jia, Q.; Zhi, D.; Dho, J.; Blamire, M. G.; MacManus-Driscoll, J. L. High-Resolution X-Ray Diffraction and Transmission Electron Microscopy of Multiferroic BiFeO₃ Films. *Appl. Phys. Lett.* **2005**, *86*, 071913.

(25) Ricinschi, D.; Yun, K.; Okuyama, M. A Mechanism for the 150 μC cm⁻² Polarization of BiFeO₃ Films Based on First-Principles Calculations and New Structural Data. *J. Phys.: Condens. Matter* **2006**, *18*, L97−L105.

(26) Rault, J. E.; Ren, W.; Prosandeev, S.; Lisenkov, S.; Sando, D.; Fusil, S.; Bibes, M.; Barthélémy, A.; Bellaiche, L.; Barrett, N. Thickness-Dependent Polarization of Strained Films with Constant Tetragonality. *Phys. Rev. Lett.* **2012**, *109*, 267601.

(27) Daumont, C. J. M.; Farokhipoor, S.; Ferri, A.; Wojdel, J. C.; Íñiguez, J.; Kooi, B. J.; Noheda, B. Tuning the Atomic and Domain Structure of Epitaxial Films of Multiferroic BiFeO₃. *Phys. Rev. B* **2010**, *81*, 144115.

(28) Wang, L.; Wang, Z.; Jin, K. J.; Li, J. Q.; Yang, H. X.; Wang, C.; Zhao, R. Q.; Lu, H. B.; Guo, H. Z.; Yang, G. Z. Effect of the Thickness of BiFeO₃ Layers on the Magnetic and Electric Properties of BiFeO₃/La₀.₇Sr₀.₃MnO₃ Heterostructures. *Appl. Phys. Lett.* **2013**, *102*, 242902.

(29) Jiang, A. Q.; Wang, C.; Jin, K. J.; Liu, X. B.; Scott, J. F.; Twang, C. S.; Tang, T. A.; Lu, H. B.; Yang, G. Z. A Resistive Memory in Semiconducting BiFeO₃ Thin-Film Capacitors. *Adv. Mater.* **2011**, *23*, 1277−1281.

(30) Wang, C.; Jin, K. J.; Xu, Z. T.; Wang, L.; Ge, C.; Lu, H. B.; Guo, H. Z.; He, M.; Yang, G. Z. Switchable Diode Effect and Ferroelectric Resistive Switching in Epitaxial BiFeO₃ Thin Films. *Appl. Phys. Lett.* **2011**, *98*, 192901.

(31) Wang, L.; Jin, C. Ge; Wang, C.; Guo, H. Z.; Lu, H. B.; Yang, G. Z. Electro−Photo Double Modulation on the Resistive Switching Behavior and Switchable Photoelectric Effect in BiFeO₃ Films. *Appl. Phys. Lett.* **2013**, *102*, 252907.

(32) Kresse, G.; Joubert, D. From Ultrasoft Pseudopotentials to the Projector Augmented-Wave Method. *Phys. Rev. B* **1999**, *59*, 1758.

(33) Dupé, B.; Infante, I. C.; Geneste, G.; Janolin, E.-E.; Bibes, M.; Barthélémy, A.; Lisenkov, S.; Bellaiche, L.; Ravy, S.; Dkhil, B. Competing Phases in BiFeO₃ Thin Films under Compressive Epitaxial Strain. *Phys. Rev. B* **2010**, *81*, 144128.

(34) Perdew, J. P.; Zunger, A. Self-Interaction Correction to Density-Functional Approximations for Many-Electron Systems. *Phys. Rev. B* **1981**, *23*, 5048.

(35) Anisimov, V. I.; Aryasetiawan, F.; Lichtenstein, A. I. First-Principles Calculations of the Electronic Structure and Spectra of Strongly Correlated Systems: The LDA+U Method. *J. Phys.: Condens. Matter* **1997**, *9*, 767−808.

(36) Kresse, G.; Furthmuller, J. Efficient Iterative Schemes for ab Initio Total-Energy Calculations Using a Plane-Wave Basis Set. *Phys. Rev. B* **1996**, *54*, 11169.

(37) Das, R. R.; Kim, D. M.; Baek, S. H.; Eom, C. B.; Zavaliche, F.; Yang, S. Y.; Ramesh, R.; Chen, Y. B.; Pan, X. Q.; Ke, X.; Rzchowski, M. S.; Streiffer, S. K. Synthesis and Ferroelectric Properties of Epitaxail BiFeO₃ Thin Films Grown by Sputtering. *Appl. Phys. Lett.* **2006**, *88*, 242904.

(38) Lichtensteiger, C.; Triscone, J.-M. Ferroelectricity and Tetragonality in Ultrathin Films. *Phys. Rev. Lett.* **2005**, *94*, 047603.

(39) Nagarajan, V.; Junquera, J.; He, J. Q.; Jia, C. L.; Waser, R.; Lee, K.; Kim, Y. K.; Baik, S. L.; Zhao, T.; Ramesh, R.; Ghosez, P.; Rabe, K. M. Scaling of Structure and Electrical Properties in Ultrathin Epitaxial Ferroelectric Heterostructures. *J. Appl. Phys.* **2006**, *100*, 051609.

(40) Gerra, G.; Tagantsev, A. K.; Setter, N.; Parlinski, K. Ionic Polarizability of Conductive Metal Oxides and Critical Thickness for Ferroelectricity in BaTiO₃. *Phys. Rev. Lett.* **2006**, *96*, 107603.